

Efficient Photonic Crystal Fiber Design for Higher OAM Modes with Low Loss Towards Next Generation THz Communication

Bibhatsu Kuri

Sidho Kanho Birsha University

Bubai Dutta

Sidho Kanho Birsha University

Nilanjana Sarkar

Sidho Kanho Birsha University

Saikat Santra

Sidho Kanho Birsha University

Paulomi Mandal

Sidho Kanho Birsha University

Khaleda Mallick

Sidho Kanho Birsha University

Ardhendu Sekhar Patra (✉ ardhendu4u@yahoo.com)

Sidho Kanho Birsha University

Research Article

Keywords: circular photonic crystal fiber (C-PCF), terahertz frequency, Finite element method, refractive index (RI)

Posted Date: August 31st, 2021

DOI: <https://doi.org/10.21203/rs.3.rs-845789/v1>

License: © ⓘ This work is licensed under a Creative Commons Attribution 4.0 International License.

[Read Full License](#)

Version of Record: A version of this preprint was published at Optical Fiber Technology on January 1st, 2022. See the published version at <https://doi.org/10.1016/j.yofte.2021.102752>.

Efficient Photonic Crystal Fiber Design for Higher OAM Modes with Low Loss towards Next Generation THz Communication

Bibhatsu Kuir¹, Bubai Dutta¹, Nilanjana Sarkar¹, Saikat Santra¹, Paulomi Mandal¹, Khaleda Mallick¹, and Ardhendu Sekhar Patra^{1*}

¹Department of Physics, Sidho Kanho Birsha University, Purulia, WB, 723104 India

*corresponding author email: ardhendu4u@yahoo.com

ABSTRACT

A newer and efficient solid core with air holes and ring based circular photonic crystal fiber (C-PCF) design is proposed, developed, and studied. The C-PCF structure with a ring core and three layers of air holes is developed to communicate terahertz frequency of the range of 1 THz to 3 THz. Finite element method (FEM) is used to optimize the position, shape and dimensions of air holes and refractive index (RI) of material for the proposed PCF design and check the efficiency to support different orbital angular momentum (OAM) modes for communication. Our novel designed C-PCF supports multiple stable modes with mode purity above 0.9. Confinement loss is in the range of 10^{-12} dB/cm, highest effective mode area in the order of 1 mm^2 is achieved in the investigated study for 3 THz transmission. The study observes that the performance of PCF is strongly dependent on RI of core and cladding.

Introduction

Photonic Crystal fibers (PCFs) is one of the most stable and secure mode of transport to transmit optical signal for next generation high speed communication systems. PCFs are considered as one of the most promising fiber technology that has very important and particular features such as controlled dispersion¹, multi-mode supports², high modes numbers and low loss³. Photonic crystal is also competent in quantum optical communication systems⁴. It is relatively least affected by external factor such as air quality, atmospheric turbulence and other common challenges faced by communication medium for wireless orbital angular momentum (OAM) based systems⁵. Space division multiplexing (SDM) technique using multi-mode fibers is an alternative to cope up with ever increasing bandwidth demand⁶. The properties of PCF can be tuned by changing the design of the fiber such as by changing the air hole patterns⁷. Photonic crystal fiber such as circular PCFs (C-PCF) has proven to be a promising candidate for the same^{2,8}. Designing modern photonic crystal and fabricating them is a real challenge⁹, thus designing a relatively simpler PCF both in terms of design components, materials, as well as fabrication process is an intensive optimization process and requiring a great deal of understanding¹⁰. The successful fabrication such as the one with hollow core silica Bragg fibers¹¹ proves that fabrication of our C-PCF architecture feasible. Because of its wide range of possible applications in optical manipulation¹², imaging¹³, quantum information¹⁴, and communications¹⁵, the OAM beam has recently sparked a lot of interest. OAM beams can be generated using different techniques¹⁶⁻¹⁸. Theoretically it is known OAM carry infinite number of modes¹⁹. Recent attraction towards research in the study of OAM of light has grown manifolds^{20,21}. The interminable demand of increasing data rates, inspire newer developments and scientific advancements in the field of communication system and PCFs provide a promising component for its solution.

In our present work we address a novel circular PCF design which is efficient, simpler, relatively easy to manufacture as well as supports higher number of modes in the THz range which are discussed and described in the results section in this paper. The proposed C-PCF has a hollow core structure. FEM is used to numerically solve the proposed model. FEM²² is a well established methodology used for numerical investigation of C-PCFs. The simulation was done in the range from 1 THz to 3 THz. The architecture is optimised with the design parameters such as the dimension and placement of the air holes and SF₂ rings to communicate higher order OAM modes. The intensity, phase and the purity of the OAM modes²³ in the PCF helps in multiplexing²⁴ of data and de-multiplexing to receive data for communication systems. More denser and pure modes will help to transmit data to long distance efficiently²⁵. The solutions are checked for convergence of the wave equations and analysed. Effective refractive index, confinement loss, dispersion, mode purity and guiding OAM Modes are studied in our proposed work to prove its potentiality. As best of our knowledge, this proposed C-PCF is one of the most flexible architecture reported in literature in terms of fabrication easiness and maximum mode guiding ability.

Proposed PCF design

We propose a hollow core C-PCF design as shown in Fig. 1, which is composed of 3 set of air hole rings and Silica/ SF_2 layers to communicate THz frequency. The innermost hollow core is filled with air (RI: 1.0) of radius $230 \mu m$ (r_1). The next layer (region 2) is made up of silica of radius $684 \mu m$ (r_2) which consists of 15 air holes ring of radius $45 \mu m$ (h_1) and another set of 15 air holes of radius $80 \mu m$ (h_2). The next layer (region 3) is composed of a complete ring with higher refractive index (RI=1.62) which is doped with SF_2 which helps to guide maximum OAM modes with low loss of radius $946 \mu m$ (r_3)²⁶. The final and outer layer (region 4) are made up of the same background material silica of radius $1261 \mu m$ (r_4). This layer also contains 24 air holes of radius $100 \mu m$ (h_3). The details of the parameter values are tabulated in Table 1. All the parameters of each component of our proposed C-PCF are designed, optimized and analysed employing FEM.

Parameters List					
Layer radius	Value	Airhole Radius	Value	Material	R.I
r_1	$230 \mu m$	h_1	$45 \mu m$	F.Silica	1.446
r_2	$684 \mu m$	h_2	$80 \mu m$	SF_2	1.62
r_3	$946 \mu m$	h_3	$100 \mu m$	Air	1
r_4	$1261 \mu m$				
r_5	$1501 \mu m$				

Table 1. Photonic Crystal Fiber design parameters

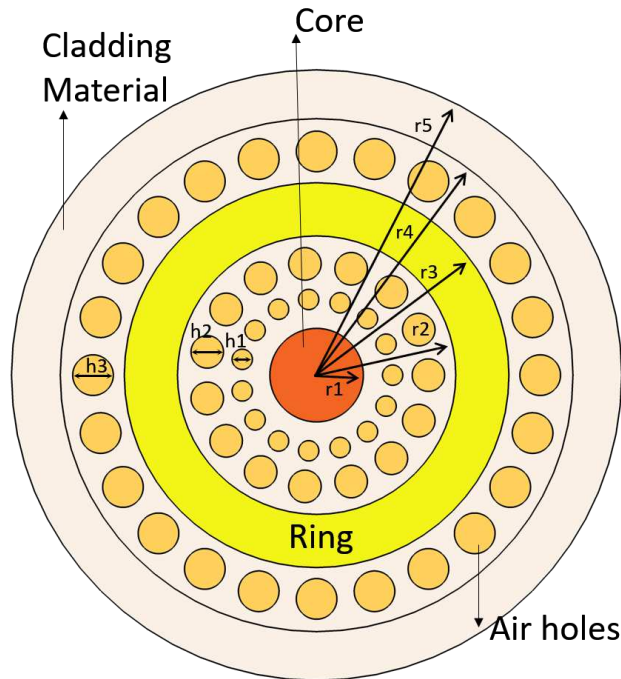


Figure 1. Cross section of the proposed C-PCF

FEM requires efficient meshing both for consistent result and reduced computation time²⁷. The meshing and details about the C-PCF geometry are shown in Fig. 2. The meshing is optimized with the input wavelength and the geometry. Tetrahedral and triangular mesh are used for meshing the model. Triangular mesh is seen to give consistent results. The limitation of the larger mesh ($\sim \lambda$) is controlled by the input wavelength and architecture of the C-PCF. The largest mesh dimension should be set according to the wavelength to reduce any inconsistency in results. In our study, given wavelength λ , minimum element size $\lambda/8$ and maximum element size 100λ are used. Element growth of 1.3 is used along with triangular meshing to fill the model

geometry as shown in the mesh Fig. 2. The meshing is needed to be reconfigured based on the refractive index, geometry of C-PCF and wavelength of light to get consistent results . A 3D view of the proposed C-PCF is shown in the Fig.3. The cross section of Fig. 3 shows the C-PCF design profile. The light is propagating along z-axis, the projection length is in the direction of the length of the fiber along which it is being fabricated.

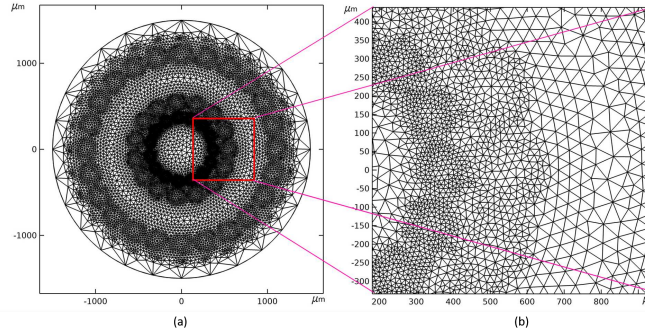


Figure 2. Mesh diagram of the proposed architecture (a) Mesh diagram of the C-PCF (b) Magnified view of the mesh (red square)

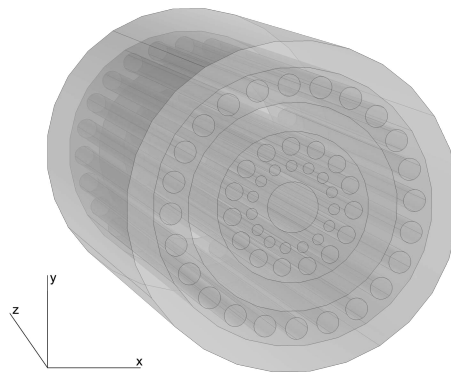


Figure 3. A 3D representation of proposed C-PCF

Theory

The fundamental theory is based on basic electromagnetic equations. The Maxwell's macroscopic property constitutive relations²⁸ of a medium with polarization P is related as

$$D = \epsilon_0 E + P \quad (1)$$

$$B = \mu_0 (H + M) \quad (2)$$

$$J = \sigma E \quad (3)$$

Where the terms are standard terms and constants. Here, D is the electric displacement and B magnetic induction. The generalized relation for modelling nonlinear materials, the electric field is represented as

$$D = \epsilon_0 \epsilon_r E + D_r \quad (4)$$

$$B = \mu_0 \mu_r H + B_r \quad (5)$$

Where D_r is the displacement field when no electric field is present. Similarly, B_r is the magnetic flux when no magnetic field is present. In terms of scalar and vector potentials, the electric and magnetic field are represented as

$$B = \nabla \times A \quad (6)$$

$$E = -\nabla V - \frac{\partial A}{\partial t} \quad (7)$$

Electric and magnetic energies are defined as standard relations

$$W_e = \int_V \left(\int_0^D E \cdot dD \right) dV = \int_V \left(\int_0^T E \cdot \frac{\partial D}{\partial t} dt \right) dV \quad (8)$$

$$W_m = \int_V \left(\int_0^B H \cdot dB \right) dV = \int_V \left(\int_0^T H \cdot \frac{\partial B}{\partial t} dt \right) dV \quad (9)$$

To understand the full electromagnetic picture between different media it is important to specify the boundary conditions. At interfaces between two media when no surface current is present, the equation can be represented as:

$$n_2 \times (E_1 - E_2) = 0 \quad (10)$$

$$n_2 \times (H_1 - H_2) = 0 \quad (11)$$

Which is followed by:

$$-n \times \left[\left(\frac{1}{\mu_r} \nabla \times E \right)_I - \left(\frac{1}{\mu_r} \nabla \times E \right)_2 \right] = n \times j\omega\mu_0 (H_1 - H_2) = 0 \quad (12)$$

The wave equation in the physics can be written for the time-harmonic and eigen-frequency problems as

$$\nabla \times \left(\frac{1}{\mu_r} \nabla \times E \right) - k_0^2 \epsilon_{re} E = 0 \quad (13)$$

In 2-Dimensional study the electric field varies with the out-of-plane wave number k_z as $E_{(x,y,z)} = \vec{E}(x,y) \exp(-ik_z z)$, the wave equation can therefore be written as the following

$$(\nabla - ik_z z) \times \left[\frac{1}{\mu_r} (\nabla - ik_z z) \times E \right] - k_0^2 \epsilon_{re} E = 0 \quad (14)$$

where z is the vector which is out of the plane (x-y plane) in the z direction. $HE_{|l|+1,m}$ and $EH_{|l|-1,m}$ are the basic OAM modes with polarization in opposite directions. This can be summarized in the form of two equations

$$OAM_{\pm l,m}^{\pm} = HE_{l+1,m}^{even} \pm jHE_{l+1,m}^{odd} \quad (15)$$

$$OAM_{\pm l,m}^{\mp} = HE_{l-1,m}^{even} \pm jHE_{l-1,m}^{odd} \quad (16)$$

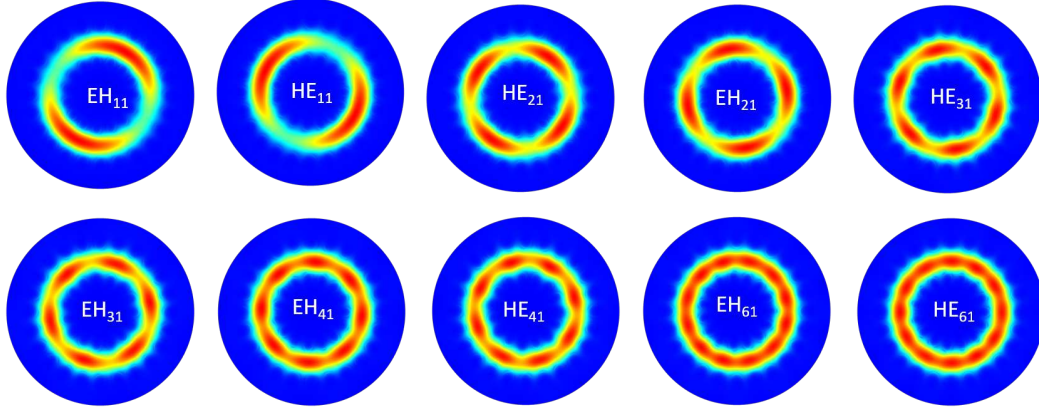


Figure 4. Intensity profile of few supported modes: (Top row) $EH_{1,1}$, $HE_{1,1}$, $HE_{2,1}$, $EH_{2,1}$ and $HE_{3,1}$. (Bottom row) $EH_{3,1}$, $EH_{4,1}$, $HE_{4,1}$, $EH_{6,1}$ and $HE_{6,1}$

Results

The 3D representation of the electric field magnitude of one of the supported mode ($HE_{1,1}$) in the fiber is shown in Fig. 5 along with the magnitude legend. The 3D profile clearly shows the confinement of the intensity profile along a ring structure and minimum intensity at the center. A 2D cross section profile of ($HE_{1,1}$) is represented in Fig. 5. The arc length represents the diameter through the center of the fiber. The y -axis represents the intensity of the field. Few of the supported modes ($HE_{1,1}$, $EH_{1,1}$, $HE_{2,1}$, $EH_{2,1}$, $HE_{3,1}$, $EH_{3,1}$, $HE_{4,1}$ and $EH_{4,1}$) from our results are shown in Fig. 4. Higher order modes are also supported in the fiber. One of the highest order modes $HE_{24,1}$ is shown in Fig. 6. Our architecture also supports the fundamental TE and TM modes.

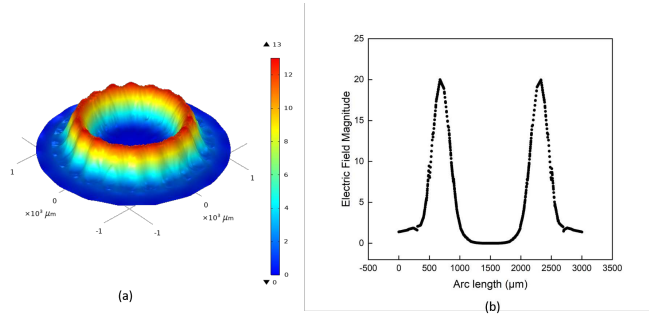


Figure 5. (a) A 3D representation of the electric field profile for $HE_{1,1}$ along with the electric field magnitude legend. (b) the electric field magnitude passing the center

Supported OAM Modes

The proposed modern C-PCF configuration design supports a wide range of modes in the THz range. The C-PCF designing specially for the THz range is crucial for next generation high bandwidth communications²⁹. The proposed design supports a large number of OAM modes as high as 80 or more modes. The frequency range of 1THz to 3THz is studied. The OAM modes are expressed as follows

$$\begin{cases} OAM_{\pm l, m}^{\pm} = HE_{l+1, m}^{even} \pm j H E_{l+1, m}^{odd} \\ OAM_{\pm l, m}^{\mp} = HE_{l-1, m}^{even} \pm j H E_{l-1, m}^{odd} \end{cases} \quad (l > 1) \quad (17)$$

$$\begin{cases} OAM_{\pm l, m}^{\pm} = HE_{l+1, m}^{even} \pm j HE_{l+1, m}^{odd} \\ OAM_{\pm l, m}^{\mp} = TM_{0, m} \pm j TE_{0, m} \end{cases} \quad (l = 0) \quad (18)$$

The superscript represented by \pm denote the circular polarization, and the “+” sign represents right circular and “-” represents

left circular polarization respectively. The supported modes for our model are listed below. It also supports the fundamental eigenmodes that is $TE_{0,1}$ and $TM_{0,1}$. Supported modes include $OAM_{\pm 1,1}^{\pm}$ ($HE_{2,1}$), $OAM_{\pm 2,1}^{\pm}$ ($HE_{3,1}, EH_{1,1}$), $OAM_{\pm 3,1}^{\pm}$ ($HE_{4,1}, EH_{2,1}$) upto $OAM_{\pm 16,1}^{\pm}$ ($HE_{17,1}, EH_{15,1}$) The plot showing few of the supported modes are shown in Fig. 4

The one of the highest order mode supported by our architecture $HE_{24,1}$ is shown in Fig. 6. The second order higher mode for $m = 2$ is also supported by the fiber. The intensity distribution in 2D and 3D height profile for the supported mode $HE_{3,2}$ are represented in Fig. 7 (a) and (b). The C-PCF design contour is also overlapped along with the field intensity. It is seen that the field is concentrated in the high index ring structure (SF_2 doped) as expected for a high mode purity profile.

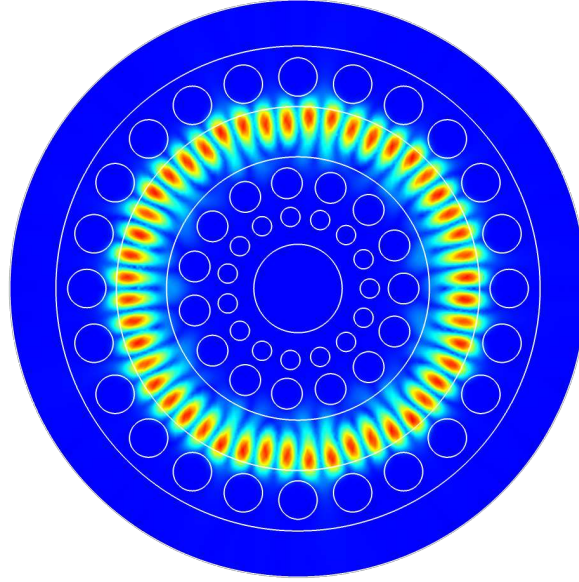


Figure 6. Field distribution of one of the high order $HE_{24,1}$ mode supported in the C-PCF

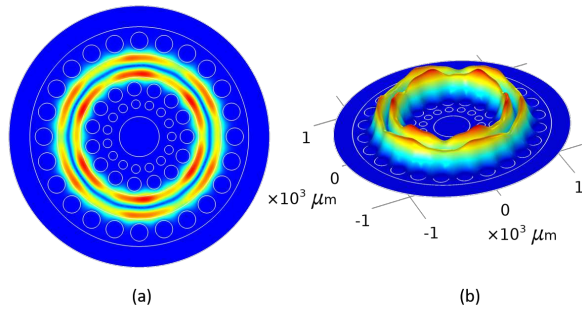


Figure 7. (a) High order $m = 2$ mode $HE_{3,2}$ profile. (b) 3D representation of intensity profile

Mode Purity

The purity of the mode is also a factor to check C-PCF transmission efficiency. Apart from seeking a greater number of OAM modes supported in the C-PCF, the designer should pay attention to the mode quality in the fibre, because it can assure high-quality stable OAM modes. The mode purity is calculated³⁰ using the eqn. (19) as

$$\eta = \frac{I_r}{I_c} = \frac{\iint_{ring} |\vec{E}|^2 dx dy}{\iint_{cross-section} |\vec{E}|^2 dx dy} \quad (19)$$

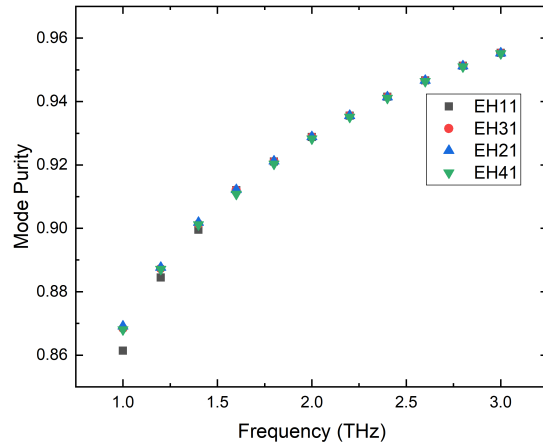


Figure 8. The mode purity at different signal frequency

Here I_r and I_c are the average mode intensity in the design and the intensity of the whole area of the C-PCF respectively. I_r is the region where all the OAM modes are expected to be confined thus the ratio is crucial for the intensity distribution of the wave. Fig.8 represents the mode purity values of few of the supported modes EH₁₁, EH₃₁, EH₂₁, EH₄₁.

Effective refractive index

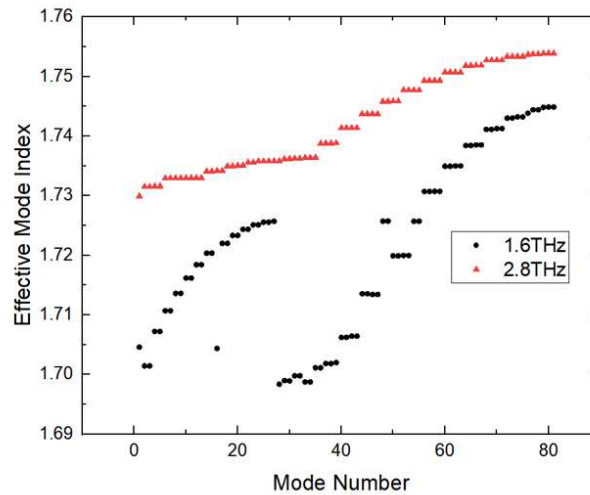


Figure 9. Variation of the effective mode index with the mode numbers

The effective refractive index (ERI) of the proposed C-PCF is optimized by FEM simulation technique. Fig. 9 shows the variation of ERI with the mode numbers. The ERI (n_{eff}) is composed of complex values and the imaginary component is many order smaller than the real part for stable modes. The values range from 1.66 to 1.76. The nature of the curve is exponential and saturates at high mode numbers, which is consistent with literature. The imaginary component contributes to the confinement loss of the C-PCF. The plot data in Fig. 9 represents the real value of the mode index along with the number of detected modes at 1.6THz and 2.8THz respectively. It can be clearly seen that points occur in pairs, indicating the two different polarizations of the same mode order EH and HE modes. We also found that the effective mode index or the ERI is higher for higher frequencies.

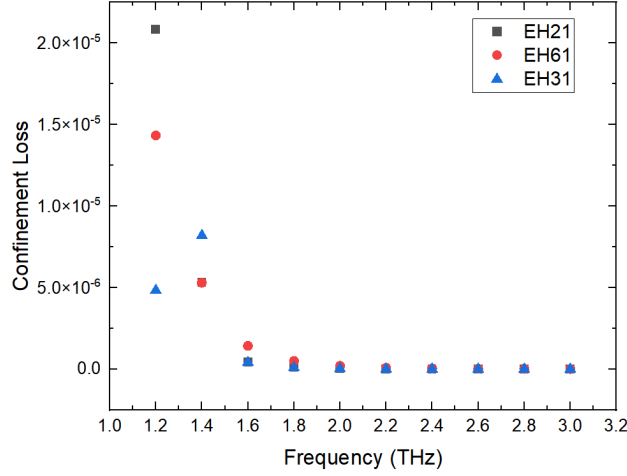


Figure 10. Confinement loss vs signal frequency

Confinement loss at THz

Confinement loss is an important parameter in any C-PCF, as it determines the loss the fiber may go through when a particular mode is transmitted through. A very few studies are being carried out at higher frequencies in the order of 1THz or higher due to the complexity and stability of results at higher frequencies. Here we calculate the confinement loss for THz range through³¹. Fig. 10 represents the confinement loss variation with frequency from 1 THz to 3 THz. The confinement loss is calculated for few of the modes $EH_{2,1}$, $EH_{3,1}$ and $EH_{6,1}$. The analysis from Fig. 10 shows the confinement loss decreases with increase in frequency. The confinement loss is calculated using the following equation.

$$C.L = \frac{2\pi}{\lambda} \frac{20}{\ln(10)} 10^6 \text{Im}(n_{eff}) \text{ (dB/m)} \quad (20)$$

Here n_{eff} represents the effective mode index, and $\text{Im}(n_{eff})$ represents the imaginary part of the effective mode index. λ is the equivalent wavelength at which the loss is measured. At 3THz the confinement loss is measured to be 9.92×10^{-11} dB/m for $EH_{2,1}$, 4.47×10^{-10} dB/m for $EH_{6,1}$ and 9.97×10^{-11} dB/m for $EH_{3,1}$ respectively.

Dispersion profile of C-PCF

Dispersion is calculated for the architecture. In a C-PCF dispersion is dominated by material dispersion and waveguide dispersion³². The dispersion of the proposed C-PCF is calculated³³ through:

$$D_{eff} = \frac{2}{c} \left(\frac{dn_{eff}}{d\omega} \right) + \frac{\omega}{C} \left(\frac{d^2n_{eff}}{d\omega^2} \right) \text{ [ps/THz/cm]} \quad (21)$$

In this equation D_{eff} is the dispersion, n_{eff} is the effective refractive index, C is the speed of light, and $\omega = 2\pi f$ where f is the frequency. The dispersion profile of the C-PCF is plotted in Fig. 11. The dispersion of four different modes $HE_{1,1}$, $HE_{2,1}$, $HE_{3,1}$ and $HE_{6,1}$ are calculated in the frequency range of 1THz to 3THz. The dispersion for $HE_{1,1}$ at 1THz is 0.1485 ps/THz/cm , $HE_{2,1}$ at 1 THz is $0.14881 \text{ ps/THz/cm}$, $HE_{3,1}$ at 1 THz is $0.14074 \text{ ps/THz/cm}$ and $HE_{6,1}$ at 1 THz is $0.17255 \text{ ps/THz/cm}$ respectively. The value decreases to $\sim 0.02 \text{ ps/THz/cm}$ at 3THz.

Effective mode area calculation

The number of guided fundamental and OAM modes through C-PCF during propagation is dependent on the effective mode area. We have designed and proposed C-PCF with largest effective mode area ($> 1.0 \text{ mm}^2$) which is much higher than the reported literature^{34,35}, as best of our knowledge. The A_{eff} value of a typical C-PCF ranges a maximum of few μm to $100\mu\text{m}$. Higher effective mode area accept higher power through C-PCF which is required for long distance transmission³⁶. From the literature is it known that, it is relatively easy to dope silica to get higher and lower refractive index, which intern impact the

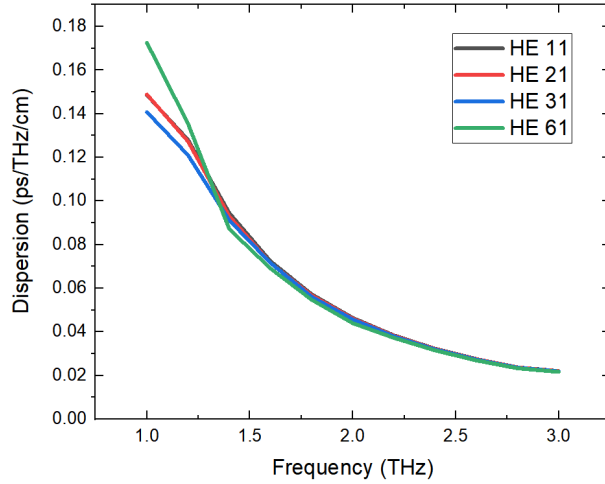


Figure 11. Dispersion of the proposed C-PCF

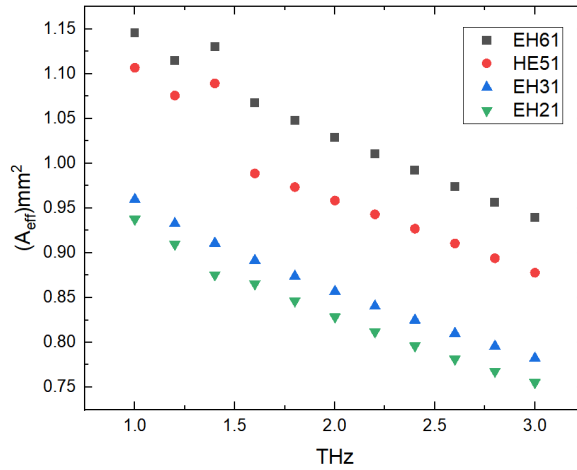


Figure 12. Variation of effective area at different frequency

effective area³⁵. The equation for standard effective mode calculations are expressed in the form:

$$A_{eff} = \frac{\left\{ \left(\int |E(x,y)|^2 dx dy \right) \right\}^2}{\iint |E(x,y)|^4 dx dy} \quad (22)$$

Fig. 12 shows the nature of the effective mode area A_{eff} for four different modes EH₂₁, EH₃₁, EH₅₁ and EH₆₁. The plot in Fig. 12 shows that A_{eff} is very high for this architecture, indicating this C-PCF is capable to work at high power intensities thus enhancing the capabilities in multimode communication systems. It is also observed the A_{eff} shows an increasing trend for higher order modes. Large mode area (LMA) C-PCFs also finds application in switching applications^{37,38}.

C-PCF stress analysis and deformation

This is the first time, we are reporting the stress analysis deformation of our proposed C-PCF. We have calculate the stress (in N/m²) over all points on the 2D cross-sectional area and plot it in the Fig. 13. As C-PCF are protected with various coatings and protective layers, it cannot avoid its own gravity and deformation due to it. At a μm scale, the deformation is quite prominent and may led to deviation for simulation results on long distance communication. The maximum stress point is found in the silica region of the outer most air hole ring. The maximum stress is found to be 69.3 N/m². The material property value is used

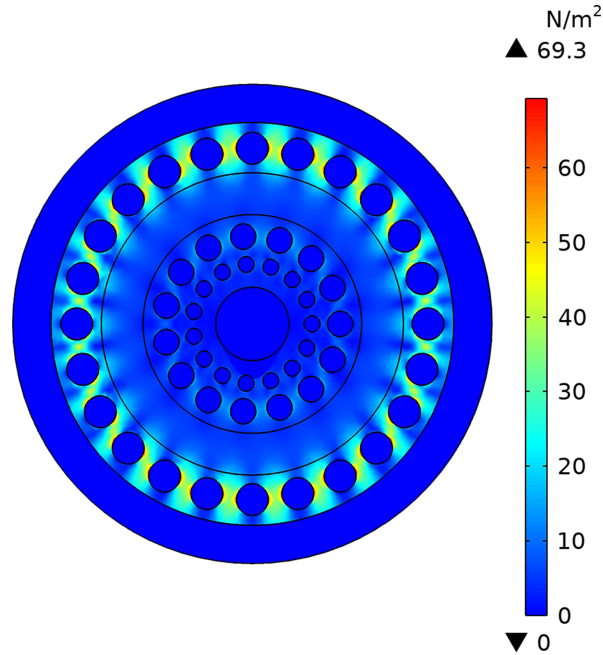


Figure 13. Stress analysis of proposed C-PCF

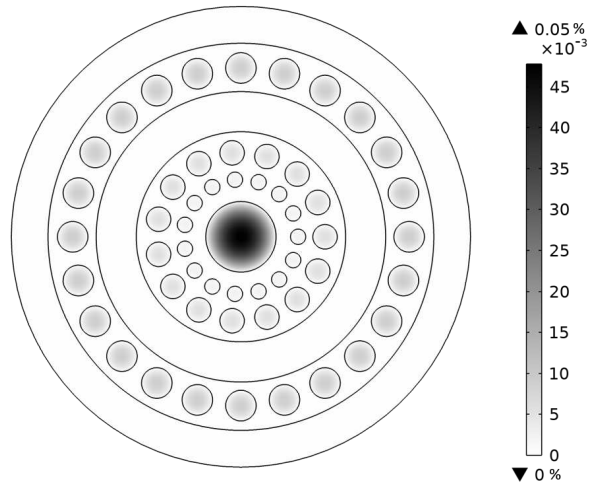


Figure 14. Relative Percentage deformation of C-PCF geometry due to gravity

to study stress analysis. Fig. 14 shows the deformation of C-PCF under the influence of gravitational force alone. From our investigation we found the deformation due to gravity is $< 1 \mu\text{m}$ which is mainly in the hollow domain containing air. For thinner C-PCF the deformation will be in the order of few nm .

Discussion

We propose a novel C-PCF with 3 air hole ring structure which supports atleast 80 OAM modes for each tested signal in the range from 1THz to 3THz using finite element method. Apart from higher supportable modes, this C-PCF also features high mode purity (>8.6), low confinement loss ($\sim 10^{-9} \text{dB/cm}$), ultra low dispersion within 10 ps/THz/cm . In addition, our proposed C-PCF also support higher order modes such as $\text{HE}_{24,1}$ and $\text{HE}_{3,2}$. High effective mode area A_{eff} along with stable and consistent effective refractive index n_{eff} are also a feature of this architecture. The simplicity in geometry and use of affordable material also indicate that it can be fabricated easily. The consistency of the fiber at various THz frequencies with

ultra low dispersion, low confinement loss and high mode purity makes our architecture stand out among the C-PCF domains. The result of the proposed C-PCF reveals that it can be applicable for next generation THz communication system.

References

1. Saitoh, K., Koshiba, M., Hasegawa, T. & Sasaoka, E. Chromatic dispersion control in photonic crystal fibers: application to ultra-flattened dispersion. *Opt. express* **11**, 843–852 (2003).
2. Zhang, L. *et al.* Circular photonic crystal fiber supporting 110 oam modes. *Opt. Commun.* **429**, 189–193 (2018).
3. Uebel, P. *et al.* Broadband robustly single-mode hollow-core pcf by resonant filtering of higher-order modes. *Opt. letters* **41**, 1961–1964 (2016).
4. Zhou, Z.-Y. *et al.* Orbital angular momentum photonic quantum interface. *Light. Sci. & Appl.* **5**, e16019–e16019 (2016).
5. Gong, L. *et al.* Optical orbital-angular-momentum-multiplexed data transmission under high scattering. *Light. Sci. & Appl.* **8**, 1–11 (2019).
6. Richardson, D. J., Fini, J. M. & Nelson, L. E. Space-division multiplexing in optical fibres. *Nat. photonics* **7**, 354–362 (2013).
7. Gregg, P. *et al.* Stable transmission of 12 oam states in air-core fiber. In *CLEO: 2013*, 1–2 (IEEE, 2013).
8. Wan, B., Zhu, L., Ma, X., Li, T. & Zhang, J. Characteristic analysis and structural design of hollow-core photonic crystal fibers with band gap cladding structures. *Sensors* **21**, 284 (2021).
9. Amouzad Mahdiraji, G. *et al.* Challenges and solutions in fabrication of silica-based photonic crystal fibers: an experimental study. *Fiber Integr. Opt.* **33**, 85–104 (2014).
10. Geerthana, S., Raja, A. S. & Sundar, D. S. Design and optimization of photonic crystal fiber with improved optical characteristics. *J. Nonlinear Opt. Phys. & Mater.* **24**, 1550051 (2015).
11. Vienne, G. *et al.* Ultra-large bandwidth hollow-core guiding in all-silica bragg fibers with nano-supports. *Opt. Express* **12**, 3500–3508 (2004).
12. Grier, D. G. A revolution in optical manipulation. *nature* **424**, 810–816 (2003).
13. Fürhapter, S., Jesacher, A., Bernet, S. & Ritsch-Marte, M. Spiral phase contrast imaging in microscopy. *Opt. Express* **13**, 689–694 (2005).
14. Nicolas, A. *et al.* A quantum memory for orbital angular momentum photonic qubits. *Nat. Photonics* **8**, 234–238 (2014).
15. Wang, J. *et al.* Terabit free-space data transmission employing orbital angular momentum multiplexing. *Nat. photonics* **6**, 488–496 (2012).
16. Huang, H. *et al.* Mode division multiplexing using an orbital angular momentum mode sorter and mimo-dsp over a graded-index few-mode optical fibre. *Sci. reports* **5**, 1–7 (2015).
17. Sueda, K., Miyaji, G., Miyanaga, N. & Nakatsuka, M. Laguerre-gaussian beam generated with a multilevel spiral phase plate for high intensity laser pulses. *Opt. express* **12**, 3548–3553 (2004).
18. Li, S. & Wang, J. Compensation of a distorted n-fold orbital angular momentum multicasting link using adaptive optics. *Opt. letters* **41**, 1482–1485 (2016).
19. Wang, X. *et al.* Recent advances on optical vortex generation. *Nanophotonics* **7**, 1533–1556 (2018).
20. Ruffato, G., Massari, M. & Romanato, F. Multiplication and division of the orbital angular momentum of light with diffractive transformation optics. *Light. Sci. & Appl.* **8**, 1–13 (2019).
21. Sroor, H. *et al.* High-purity orbital angular momentum states from a visible metasurface laser. *Nat. Photonics* **14**, 498–503 (2020).
22. Reddy, J. N. *Introduction to the finite element method* (McGraw-Hill Education, 2019).
23. Wang, L., Corsi, A., Rusch, L. A. & LaRochelle, S. Investigation of orbital angular momentum mode purity in air-core optical fibers. In *2016 IEEE Photonics Society Summer Topical Meeting Series (SUM)*, 203–204 (IEEE, 2016).
24. Fu, H. *et al.* Multiplexing of polarization-maintaining photonic crystal fiber based sagnac interferometric sensors. *Opt. express* **17**, 18501–18512 (2009).
25. Li, S. & Wang, J. Multi-orbital-angular-momentum multi-ring fiber for high-density space-division multiplexing. *IEEE Photonics J.* **5**, 7101007–7101007 (2013).

26. Al-Zahrani, F. A., Kabir, M. *et al.* Ring-core photonic crystal fiber of terahertz orbital angular momentum modes with excellence guiding properties in optical fiber communication. In *Photonics*, vol. 8, 122 (Multidisciplinary Digital Publishing Institute, 2021).
27. Andonegui, I. & Garcia-Adeva, A. J. The finite element method applied to the study of two-dimensional photonic crystals and resonant cavities. *Opt. express* **21**, 4072–4092 (2013).
28. Mansuripur, M. & Zakharian, A. R. Maxwell's macroscopic equations, the energy-momentum postulates, and the lorentz law of force. *Phys. Rev. E* **79**, 026608 (2009).
29. Yang, T., Ding, C., Ziolkowski, R. W. & Guo, Y. J. Achieving a terahertz photonic crystal fiber with enhanced birefringence. In *2020 4th Australian Microwave Symposium (AMS)*, 1–2 (IEEE, 2020).
30. Zhang, H. *et al.* A design strategy of the circular photonic crystal fiber supporting good quality orbital angular momentum mode transmission. *Opt. Commun.* **397**, 59–66 (2017).
31. Maji, P. S. & Roy Chaudhuri, P. Circular photonic crystal fibers: numerical analysis of chromatic dispersion and losses. *Int. Sch. Res. Notices* **2013** (2013).
32. Hu, Z.-A. *et al.* Photonic crystal fiber for supporting 26 orbital angular momentum modes. *Opt. express* **24**, 17285–17291 (2016).
33. Islam, M. S. *et al.* A novel approach for spectroscopic chemical identification using photonic crystal fiber in the terahertz regime. *IEEE Sensors J.* **18**, 575–582 (2017).
34. Mortensen, N. A. Effective area of photonic crystal fibers. *Opt. Express* **10**, 341–348 (2002).
35. Chen, M.-Y. Polarization and leakage properties of large-mode-area microstructured-core optical fibers. *Opt. express* **15**, 12498–12507 (2007).
36. Jin, W., Ju, J., Ho, H. L., Hoo, Y. L. & Zhang, A. Photonic crystal fibers, devices, and applications. *Front. Optoelectronics* **6**, 3–24 (2013).
37. Zografopoulos, D., Ptilakis, A. & Kriezis, E. Liquid crystal-infiltrated photonic crystal fibres for switching applications. *Optofluidics, Sensors Actuators Microstruct. Opt. Fibers* 55–83 (2015).
38. Cucinotta, A., Poli, F. & Selleri, S. Design of erbium-doped triangular photonic-crystal-fiber-based amplifiers. *IEEE Photonics Technol. Lett.* **16**, 2027–2029 (2004).

Acknowledgements (not compulsory)

We would like to acknowledge Sidho-Kanho-Birsha University, Purulia, India for providing the infrastructural facility and SERB Govt. of India (CRG/2019/006580) for supporting financially to carry out the research

Author contributions statement

All authors have contributed to design the proposed configuration. Bibhatsu Kuri performs the whole numerical analysis and prepares the manuscript. Bibhatsu Kuri, Bubai Dutta, Nilanjana Sarkar, Saikat Santra, Paulomi Mandal, and Khaleda Mallick analyses all data. All authors discussed the results and contributed to the final manuscript. Dr. Ardhendu Sekhar Patra (corresponding author) investigates and supervised the findings of this work and contributes to the writing of the manuscript.

Additional information

The authors declare that they have no known competing financial interests or personal relationships that could have appeared to influence the work reported in this paper.

Competing interests

The author(s) declare no competing interests.